Journal of Metals, Materials and Minerals, 35(2), e2348, 2025

Regulating CoP_x/Co heterostructures for enhanced electrocatalytic activity toward hydrazine oxidation reaction

Qinquan LIN[1], Rui ZHANG[2], Changli YAN[3], Qizhao HU[2], Shangbin SANG[2,*], Qiumei WU[1,*], Kaiyu LIU[2], and Hongtao LIU[2]

[1] *State Key Laboratory of Powder Metallurgy, Central South University, Changsha 410083, China*
[2] *Hunan Provincial Key Laboratory of Chemical Power Sources, College of Chemistry and Chemical Engineering, Central South University, Changsha, 410083, China*
[3] *Hangzhou Win-Win Technology Co. LTD, No. 157, Yunqi Road, Tongjun Street, Tonglu County, Hangzhou, China*

***Corresponding author e-mail**: wuqiumei@csu.edu.cn, sangshangbin@csu.edu.cn

Received date:
5 March 2025
Revised date:
17 March 2025
Accepted date:
4 April 2025

Keywords:
Electrocatalyst;
Heterostructure;
Hydrazine oxidation reaction;
Electrodeposition

Abstract

Hydrazine hydrate ($N_2H_4 \cdot H_2O$) is considered an ideal fuel for fuel cells. Constructing a cobalt phosphide/cobalt (CoP_x/Co) heterostructure can achieve efficient electrocatalytic activity for hydrazine oxidation reaction. Traditional strategies for constructing CoP_x/Co heterostructures took less consideration on the exposure of the active sites. In this study, 3D nanoflower-like nano CoP_x/Co heterostructures with highly exposed active sites were obtained on a nickel foam (NF) through a dual-component phosphating strategy, i.e., regulating the relative content of Co and $Co(OH)_2$ with cathodic current density and utilizing the differences in their phosphating behaviors. The potential at 100 $mA \cdot cm^{-2}$ and Tafel slope of the optimized CoP_x/Co(375)@NF electrode prepared with the cathodic current density of 375 $mA \cdot cm^{-2}$ are –37.4 mV (vs.RHE) and 58.9 $mA \cdot dec^{-1}$, respectively, in a 0.2 M $N_2H_4 \cdot H_2O$ solution. The stable potential was maintained after 12 h under a high current density of 100 $mA \cdot cm^{-2}$. The superior electrocatalysis activity toward $N_2H_4 \cdot H_2O$ is proved closely relative with the constructing of CoP_x/Co heterostructure. This study provides a new strategy for the development of efficient hydrazine oxidation catalysts by using a dual-component phosphating approach to fully expose the active sites of the CoP_x/Co heterostructure.

1. Introduction

With the development of the society, the concept of sustainable development has gradually become the mainstream, the development of clean energy has become more and more important [1-3]. Fuel cells, distinguished by their superior energy conversion efficiency and eco-friendliness, are considered as one of the important direction of the future energy system [4-6]. Traditional hydrogen fuel cells are clean and environmentally friendly, but hydrogen storage and transportation are relatively difficult. At the same time, they face high costs and application risks [7-9]. Organic small molecules, such as methanol and formic acid, are used as liquid fuels, and the storage and transportation conditions are relatively convenient, but in practical application, it is still faced with the problem that precious metal catalysts are needed and carbon containing products are easy to cause catalyst poisoning [10-13]. Hydrazine hydrate ($N_2H_4 \cdot H_2O$), although it faces the problems of relatively high raw material cost and toxicity, the favorable characteristics of lower oxidation potential ($N_2H_4 + 4OH^- - 4e \rightarrow N_2 + 4H_2O$, –0.33V vs. RHE), higher specific energy, and carbon-free products make it a suitable fuel choice [14-18].

Hydrazine oxidation reaction (HzOR) is a four-electron process involving multi-step reaction [19]. Among the current catalysts toward HzOR, transition metal phosphides have superior catalytic activity than platinum-based precious metal catalysts, and better stability compared to transition metals, such as nickel and cobalt, they have been considered as one of the most promising catalysts toward HzOR [20,21]. To enhance the catalytic activity of this transition metal phosphides, the construction of heterostructures is considered an important mean. For instance, after electrodeposition, hydrothermal treatment and finally phosphating, the CoNiP-Ni heterostructures were constructed on the surface of nickel foam (NF), which not only increases the loading of active materials, but also promotes electron transfer, thereby improving its catalytic activity toward hydrogen evolution reaction [22]. Wang *et al.* synthesized a composite of CoP and Co nanoparticles on the surface of the carbon layer by gas-solid photostatting Co particles which prepared by pyrolyzing Prussian blue analogues, and found the Mott-Schottky heterojunction composed of CoP and Co promoted the flow of electrons at the CoP/Co interface, thereby achieving the excellent catalytic activity toward HzOR. Density functional theory (DFT) calculations shows that the interface of the CoP/Co heterostructure not only serves as the active site for HzOR, but also facilitates the multi-step dehydrogenation for N_2H_4, thereby enhancing the activity toward HzOR, and its activity is superior than that of CoP catalysts [23]. Currently, the construction of CoP/Co heterostructure is usually prepared by pyrolyzing metal organic cobalt precursor to form metal Co particles, and then phosphating. In the phosphating process, the formation of CoP/Co heterojunction is usually limited to the carbon matrix coated on metal cobalt particles, which undoubtedly makes the active sites exposed limited [24-26].

To address the aforementioned issues, the $Co/Co(OH)_2$ heterojunction was constructed on the surface of carbon supported Co particles by hydrothermal reaction. During phosphidation in a PH_3 atmosphere, $Co(OH)_2$ and metallic Co exhibit different phosphidation behaviors: $Co(OH)_2$ is converted to CoP, while metallic Co is only partially phosphidated to form a small amount of Co_2P on the surface, thus, a $(CoP-Co_2P)/Co$ heterostructure with a core-shell structure were ultimately obtained. This heterostructure enhances the number of active sites, and improves the catalytic activity for both hydrogen evolution reaction (HER) and oxygen evolution reaction (OER), making it a promising bifunctional catalyst [27]. However, the formation of core-shell structures such as CoPx/Co is highly sensitive to the thickness of the $Co(OH)_2$ layer. If the thickness is not precisely controlled, an excessively thick phosphidation layer may form, leading to insufficient exposure of active sites in the heterojunction. Thus, the controllable formation of $Co/Co(OH)_2$ heterojunction becomes important.

During the electrochemical deposition of metallic cobalt in neutral solution, the hydrogen evolution reaction (HER) as an associated reaction increases the pH of solution on electrode surface, $Co(OH)_2$ and Co can be co-deposited in situ on a substrate to directly form a $Co/Co(OH)_2$ heterojunction precursor [28]. On the other hand, during the process of electrodeposition metal Co coating, it is found that the grain size, morphology and the ratio of Co to $Co(OH)_2$ could be controlled by adjusting the cathodic current density [29,30].

In present paper, a self-supported three-dimensional (3D) nanostructure precursor of $Co/Co(OH)_2$ was electrodeposited onto the surface of NF by optimization the cathodic current density. The CoPx/Co@NF electrodes with CoPx/Co heterostructure and adjustable microstructure were prepared after phosphorization. The catalytic activity and stability toward HzOR in 0.2 M $N_2H_4{\cdot}H_2O$ + 1 M KOH solution of the prepared catalysts were evaluated, and the mechanism of the catalytic behavior was discussed.

2. Experimental sections

2.1 Materials

Hydrochloric acid (HCl), ethanol, hydrazine monohydrate ($N_2H_4{\cdot}H_2O$, 80 wt%), cobalt(II) chloride hexahydrate ($CoCl_2{\cdot}6H_2O$), cobalt(II) nitrate hexahydrate ($Co(NO_3)_2{\cdot}6H_2O$) and ammonium chloride (NH_4Cl) were all bought from the National Pharmaceutical Group Chemical Reagent Co., Ltd. Sodium hypophosphite (NaH_2PO_2) was obtained from Aladdin. Potassium hydroxide (KOH) was purchased from Shanghai Titan and nickel foam (thickness: 1 mm; pore diameter: 0.1 mm; porosity: 97%) was acquired from Saibo Electronics Co., Ltd.

2.2 Electrode preparations

2.2.1 Pre-treatment of nickel foam

Firstly, nickel foam (NF) was cut into pieces of 1 cm × 1.5 cm and sonicated for 10 min in anhydrous ethanol, 6 M hydrochloric acid and distilled water, successively. Subsequently, the nickel pieces were placed in vacuum drying oven and dried at 80°C for 2 h.

2.2.2 Preparation of CoPx/Co@NF electrodes

The preparation process of the CoP_x/Co@NF electrode is shown in Figure 1. Electrochemical deposition was performed using chronoamperometry with a constant charge density of $I \times t = 25000$ mA·s in a solution of 2 M NH_4Cl + 0.1 M $CoCl_2$ [29]. The current densities of the deposition process were 50, 250, 375, 500 and 625 $mA{\cdot}cm^{-2}$, respectively. The corresponding precursors obtained were denoted as $Co/Co(OH)_2(x)$@NF, where x is presented the current density. Then the phosphorus source NaH_2PO_2 and the obtained precursor $Co/Co(OH)_2$@NF were placed in two independent positions in the long crucible, wherein 200 mg NaH_2PO_2 was in the upstream side of the tubular furnace and the precursor was on the other side. Subsequently, under argon atmosphere, the temperature was ramped up to 325°C at a rate of $2°C{\cdot}min^{-1}$ and held for 4 h. After cooling down to room temperature under argon, the $CoP_x/Co(x)$@NF electrodes were obtained, where x is denoted as the current density. Besides, the $CoP_x/Co(375)/Ti$ electrode was prepared with the same process as those for the $CoP_x/Co(375)$@NF electrode, then the powder was peeled off from the titanium sheet and used for phase characterization.

The phosphidation degree for the $CoP_x/Co(x)$@NF electrode is assessed by the phosphidation index y , which was defined as

$$y = [(m_3 - m_2)/(m_2 - m_1)] \times 100\% \qquad (1)$$

Where m_1, m_2, and m_3 are the masses of NF substrate, $Co/Co(OH)_2(x)$@NF precursor and $CoP_x/Co(x)$@NF electrode, respectively.

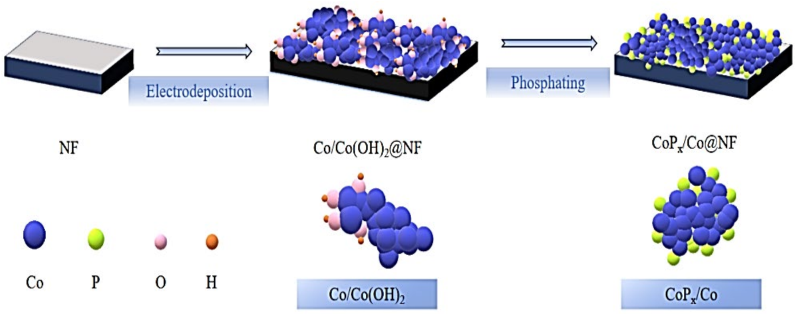

Figure 1. Schematic diagram of the preparation process for CoPx/Co@NF electrode.

2.2.3 Preparation of the NF-P and CoP@NF electrodes

A sample, designated as NF-P, was obtained by phosphorizing a clean NF under the same phosphated process as those for the CoP_x/Co(x)@NF electrodes. Another sample, CoP@NF, was obtained by depositing only $Co(OH)_2$ precursor on the NF surface in 0.1 M $Co(NO_3)_2$ solution at the optimized current density of 75 mA·cm^{-2} for 100 s [31], followed by phosphorization under the same conditions as those for the CoP_x/Co@NF electrodes.

2.3 Electrochemical characterization

All electrochemical characterizations were conducted on DH7000 electrochemical workstation. Ag/AgCl electrode and platinum (Pt) sheet served as the reference electrode and counter electrode, respectively. The Ag/AgCl electrode was stored in a saturated KCl solution and rinsed with deionized water before use. The linear sweep voltammetry (LSV) measurements were performed in 0.2 M $N_2H_4·H_2O$ + 1 M KOH solution with the scan rate of 10 mV·s^{-1} and 85% iR_1 compensation ($E_{corrected} = E_{measured} - 85\% \ iR_1$) was applied, where the solution resistance R_1 was obtained from electrochemical impedance spectroscopy (EIS) data fitting. The EIS measurements were performed at the open-circuit potential over a frequency range of 10^{-1} Hz to 10^6 Hz. Tafel plots were derived from the Tafel equation $\eta = a \log|i| + b$. The stability of the electrodes was evaluated using the chronoamperometry in 3 M $N_2H_4·H_2O$ + 1 M KOH solution. If not otherwise specified, all the potentials reported in this study were converted to the reversible hydrogen electrode (RHE) and the conversion formula is $E_{RHE} = E_{measured} + 0.198 + 0.059$ pH, and the scanning rate is 10 mV·s^{-1}.

2.4 Phase characterization

The phase characterization of the sample was performed by X-ray diffraction (XRD; Phillips Xpert-MPD PW3040 diffractometer). The morphology of the samples were characterized by field-emission scanning electron microscope (FE-SEM; Nova NanoSEM 230). Additionally, the elemental compositions and distributions of the samples were analyzed by an energy-dispersive spectrometer (EDS mapping). The elemental composition and valence states of the samples were analyzed through X-ray photoelectron spectroscopy (XPS, Thermo Scientific ESCALAB 250Xi) with an aluminum Kα X-ray source. The binding energy of XPS spectra was calibrated using C1s (284.6 eV).

3. Results and discussion

3.1 Structures of the CoP_x/Co@NF electrode

In order to confirm the structure of the CoP_x/Co(375) powders, the CoP_x/Co(375)/Ti electrode was prepared with the same method as those for the CoP_x/Co(375)@NF, then the powder was peeled off from the titanium sheet and used for phase characterization. As shown in Figure 2, the CoP_x/Co(375) powder exhibits characteristic diffraction peaks corresponding to Co_2P, CoP and metallic Co. Specifically, the peaks centered at 40.77°, 53.29° and 52.10° are assigned to the (121), (211), and (230) planes of Co2P (PDF#00-032-0306). The peak at 56.0° corresponds to the (211) plane of CoP (PDF#00-029-0497). The peaks at 41.60°, 44.39°, 47.36° and 75.88° are attributed to the (100), (002), (101) and (110) planes of metallic Co (PDF#00-005-0727). The XRD pattern indicates that the phosphated material is a mixture of Co_2P, CoP and Co phases, confirming the formation of a CoP_x/Co hetero-structure with elemental cobalt and cobalt phosphides. It is worth noting that during the phosphating process, the obtained CoP_x is prone to further oxidation to form phosphates [32], but no relevant phases were detected, which means that the phosphides produced on this surface may be rare or amorphous.

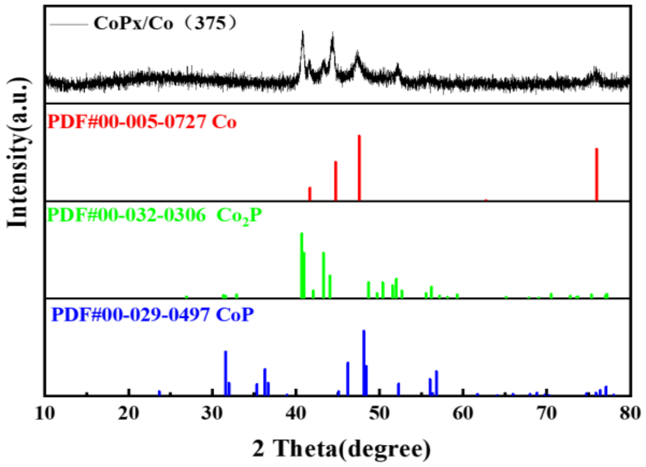

Figure 2. XRD patterns of CoP_x/Co(375) powder.

3.2 Morphology and element distribution of CoP_x/Co(x)@NF electrodes

SEM images and EDS mapping of Co/$Co(OH)_2$(375)@NF, CoP_x/Co(375)@NF and CoP@NF electrodes are shown in Figure 3(a-c). The uniform and similar distributions of Co and P elements on the surface of CoP_x/Co(375)@NF and CoP@NF indicate that phosphorus was incorporates into the precursors successfully via the gas-solid phosphidation. The presence of oxygen elements might come from the phosphates. Comparing with the SEM images of the CoP_x/Co(375)@NF, which shows stacked nanosheets, forming a nanoflower-like structure, the precursor Co/$Co(OH)_2$(375)@NF electrode exhibits a surface composed of stacked lamellar floccules. This transformation illustrates that the introduction of P elements leads to the rearrangement of atoms on the electrode surface, causing the change in the electrode morphology from lamellar floccules to nanosheets, ultimately forming the nanoflower-like structure. Compared with the SEM image of CoP_x/Co(375)@NF electrode, the CoP@NF electrode (Figure 3(c)) shows the loose material of nanosheets, does not form an ordered nano-flower structure. Meanwhile, Co and P elements are evenly distributed on the surface. Compared with the SEM images for the CoP_x/Co(x)@NF electrodes with different cathodic current density shown in Figure 3(d-f), as the deposition current increases from 50 mA·cm^{-2} to 375 mA·cm^{-2}, the surface morphology of the CoP_x/Co film changes from a layered honeycomb structure to a nanoflower-like structure. When the deposition current further increases to 625 mA·cm^{-2}, the original nanoflower structure gradually disappears and transforms into a large nanosheet structure. This indicates that the morphology of the CoP_x/Co nanoarray can be regulated by adjusting the deposition current density. Among the three morphologies, the nanoflower-like structure undoubtedly possesses the highest specific surface area, which not only exposes more active sites on the surface, but also facilitates the mass transfer.

The atomic ratios of Co, P and O elements in the EDS mapping results for the electrodes were listed in Table 1. The results show the phosphorus content and the P:Co atomic ratio on the electrode surface increase as the cathodic current density increases. The reason might be that with the deposition current density increases, the size of crystalline grain of the precursor particles might become smaller and the proportion of $Co(OH)_2$ in the precursor increases [33], While during phosphidation process, $Co(OH)_2$ reacts more readily with the generated PH_3 gas ($Co(OH)_2 + PH_3 \rightarrow CoP + H_2O$) compared to metallic Co [27]. As a result, electrodes with smaller grains and a higher proportion of $Co(OH)_2$ are more easily phosphidated, leading to an increase in phosphorus content on the particle surface, that is, by selecting an appropriate cathodic current density for precursor deposition, the morphology of the CoP_x/Co film and the amount of phosphorus, as well as the CoP_x/Co ratio can be controlled. On the other hand, the atomic ratio of P:Co on the surface of CoP_x/Co@NF electrodes is lower than that of CoP@NF electrodes, which further indicates that only part of the metallic Co particles in the $Co/Co(OH)_2$@NF precursor can be phosphidated and $Co(OH)_2$ reacts more readily with the generated PH_3 gas.

3.3 Phosphorization degrees of CoP_x/Co@NF electrodes

The phosphidation degrees for the $CoP_x/Co(x)$@NF electrodes were assessed by the phosphidation index y. A higher value of y indicates a deeper degree of phosphidation. As shown in Figure 4, the phosphidation index y rises as the cathodic current density increases, which is consistent with the results of EDS mapping and further shows that as the cathodic current density increases, the Co particles become finer, the content of $Co(OH)_2$ increases, which might both contribute to the higher phosphidation degree.

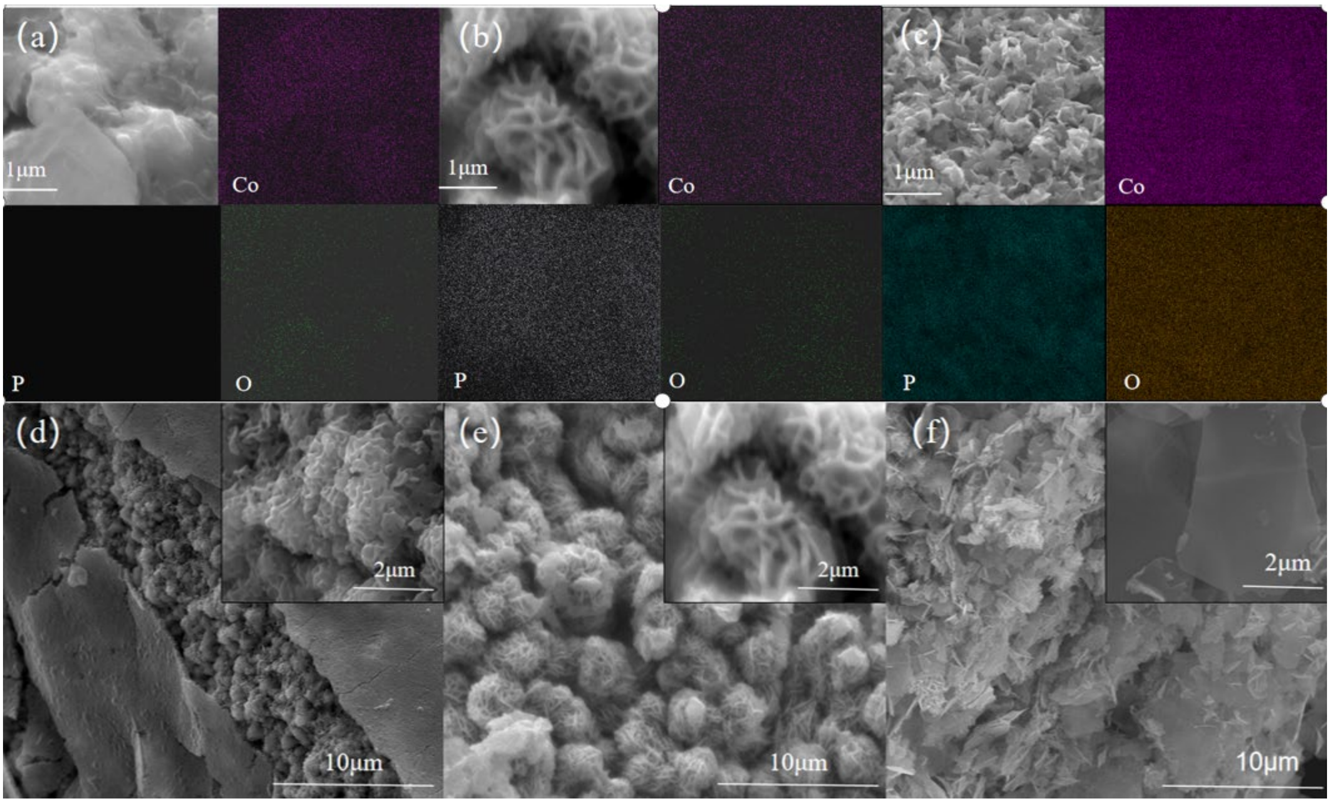

Figure 3. SEM images and EDS mappings of (a) $Co/Co(OH)_2(375)$@NF, (b) $CoP_x/Co(375)$@NF, and (c) CoP@NF electrodes; SEM image of, (d) $CoP_x/Co(50)$@NF, (e) $CoP_x/Co(375)$@NF, and (f) $CoP_x/Co(625)$@NF electrodes.

Table 1. Atomic ratios of Co, P, and O elements in the EDS mapping results for the electrodes.

Electrodes	**Co [at%]**	**P [at%]**	**O [at%]**	**P/Co**
$CoP_x/Co(50)$@NF	79.94	9.98	10.08	0.12
$CoP_x/Co(375)$@NF	71.48	12.90	15.62	0.18
$CoP_x/Co(625)$@NF	36.24	27.09	36.67	0.75
CoP@NF	24.00	26.50	49.50	1.10
$Co/Co(OH)_2(375)$@NF	94.40	-	5.60	-

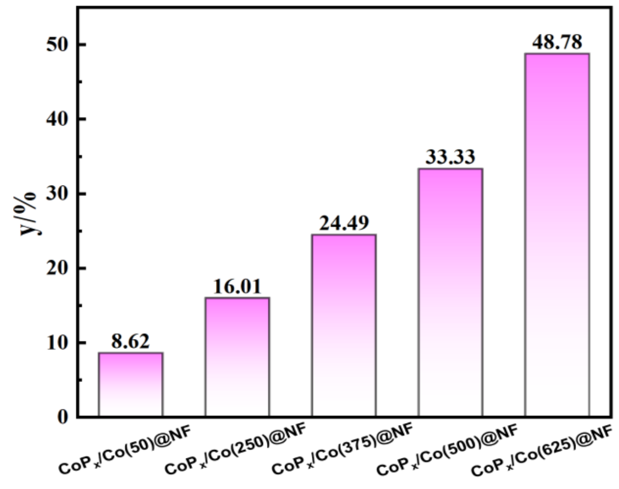

Figure 4. The phosphorization degrees for CoP$_x$/Co(x)@NF electrodes.

3.4 Valence analysis of elements for CoP$_x$/Co(x)@NF and Co/Co(OH)$_2$(375)@NF electrodes

Figure 5(a) shows the XPS full spectra of CoP$_x$/Co(375)@NF and Co/Co(OH)$_2$(375)@NF electrodes. Compared with that for the Co/Co(OH)$_2$(375)@NF electrode, the full XPS spectrum of the CoP$_x$/Co(375)@NF electrode exhibits an additional P 2p peak, which indicates the successful incorporation of phosphorus into the electrode surface. Figure 5(b) presents the high-resolution XPS spectra of Co 2p3/2 for the CoP$_x$/Co(50)@NF, CoP$_x$/Co(375)@NF and CoP$_x$/Co(625)@NF electrodes. The peaks centered at about 779.02 eV, 782.63 eV, and 786.13 eV belong to metallic Co, cobalt phosphides (CoP$_x$) and cobalt phosphate (CoPO$_x$), respectively [27,34,35], and the peak around at about 790.37 eV is attributed to satellite peak of Co2p3/2 [24]. The presence of CoPO$_x$ is the result of the oxidation of CoP$_x$ species exposed in the atmosphere in the subsequent process and the presence of metallic Co and CoP$_x$ suggests the successful construction of the CoP$_x$/ Co heterojunction on the electrode surface [23,36]. The corresponding histograms for the ratios of Co, CoP$_x$ and CoPO$_x$ for the CoP$_x$/Co(50) @NF, CoP$_x$/Co(375)@NF and CoP$_x$/Co(625)@NF electrodes are provided in Figure 5(d). It can be seen that as the cathodic current density increases, the relative content of metallic Co on the surface gradually decreases, while the contents of CoP$_x$ and CoPO$_x$ both enhanced, which is consistent with the previous EDS mapping results, i.e., phosphidation degree increases with the increasing cathodic current density as shown in Table 1. It can be concluded that the higher cathodic current density, the finer particle and more Co(OH)$_2$ would be formed for the precursor, which might contributed to the higher oxidation degrees from metallic Co to CoP$_x$ and from CoP$_x$ to CoPO$_x$. Figure 5(c) is the high-resolution XPS spectra of P 2p for the CoP$_x$/ Co(x)@NF with different cathodic current density. Peaks centered at about 130.96 eV and 134.27 eV are considered to come from metal phosphides and phosphate (PO$_x$) due to the oxidation of phosphides in air [35,37]. It is obvious that content of metal phosphides of CoP$_x$/Co(375)@NF with the cathodic current density be 375 mA·cm^{-2} is higher than the other two, which would be benefit to the formation of the CoP$_x$/Co heterojunction.

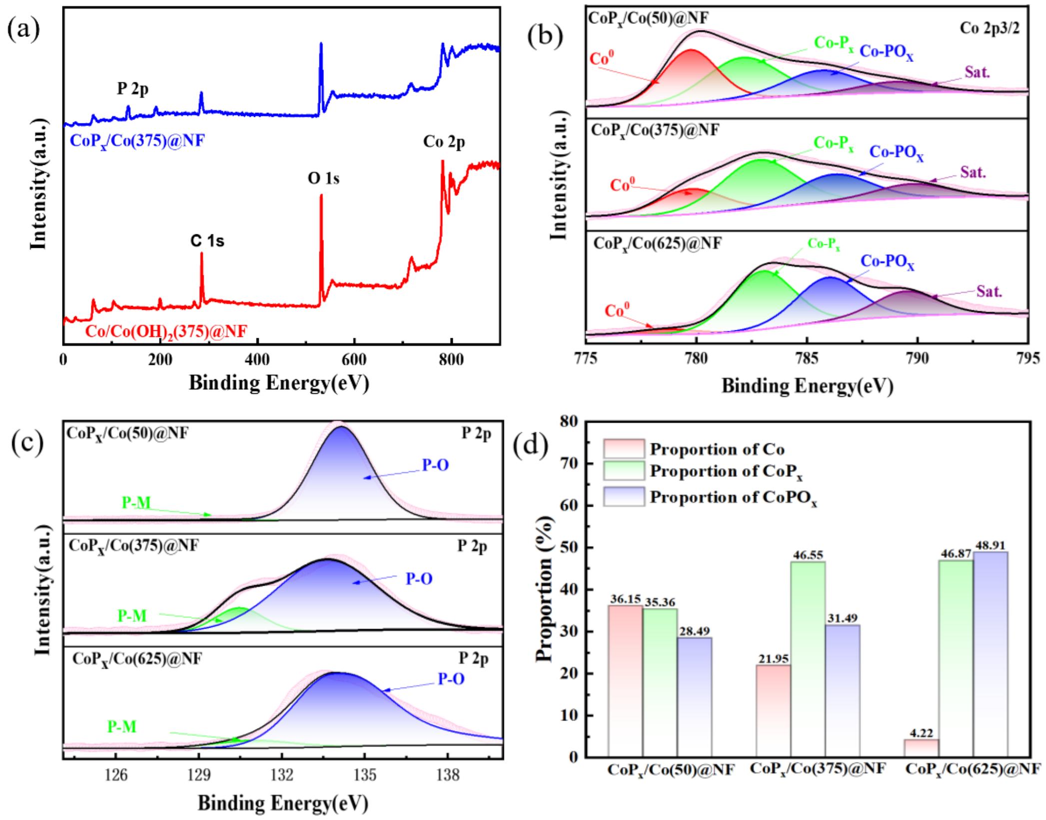

Figure 5. (a) XPS full spectra of CoP$_x$/Co(375)@NF and Co/Co(OH)$_2$(375)@NF electrodes; High-resolution XPS spectra of, (b) Co 2p3/2, and (c) P 2p for the CoP$_x$/Co(50)@NF, CoP$_x$/Co(375)@NF and CoP$_x$/Co(625)@NF electrodes, (d) Histograms of the corresponding ratios of Co, CoP$_x$ and CoPO$_x$ for the CoP$_x$/Co(x) @NF electrodes**.**

3.5 Electrochemical catalytic activity toward HzOR

The LSV curves of the NF-P, CoP@NF and $CoP_x/Co(x)$@NF electrodes prepared at different cathodic current density in the 0.2 M $N_2H_4{\cdot}H_2O$ + 1 M KOH solution are present in Figure 6(a). The NF-P sample show almost no significant changes during the whole applied potential, indicating that the NF-P substrate itself has negligible catalytic activity towards HzOR, while the presence of the CoP_x/Co heterostructure enhances the catalytic activity towards HzOR obviously and it is clear that the cathodic current density used for $Co/Co(OH)_2$ deposition significantly affects the activity toward HzOR. Among them, the $CoP_x/Co(375)$@NF electrode exhibits the best catalytic property. As shown in Figure 6(b), with the deposition current density increases from 50 $mA{\cdot}cm^{-2}$ to 375 $mA{\cdot}cm^{-2}$, the catalytic activity toward HzOR of the electrodes increases, with the potential shift negatively from 19.1 mV@100 $mA{\cdot}cm^{-2}$ to –37.6 mV@100 $mA{\cdot}cm^{-2}$, then shifts positively to –12.4 mV@100 $mA{\cdot}cm^{-2}$ as the deposition current density further increase to 625 $mA{\cdot}cm^{-2}$. Figure 6(c) shows that the $CoP_x/Co(375)$@NF electrode exhibits the lowest Tafel slope of 58.9 $mA{\cdot}dec^{-1}$, which shows that the fast catalytic kinetics for HzOR might be relative with its suitable morphology and phosphidation degree, that is, insufficient phosphidation at low depositing current density leads to a lack of active sites, and excessive phosphidation at high depositing current density results in over-encapsulation of Co active sites by phosphates, thereby limiting their exposure. Though the CoP@NF electrode shows catalytic activity toward the HzOR, but it shows only comparable activity with the $CoP_x/Co(50)$@NF compared, which further indicating CoP_x/Co heterojunction play a key role for the HzOR.

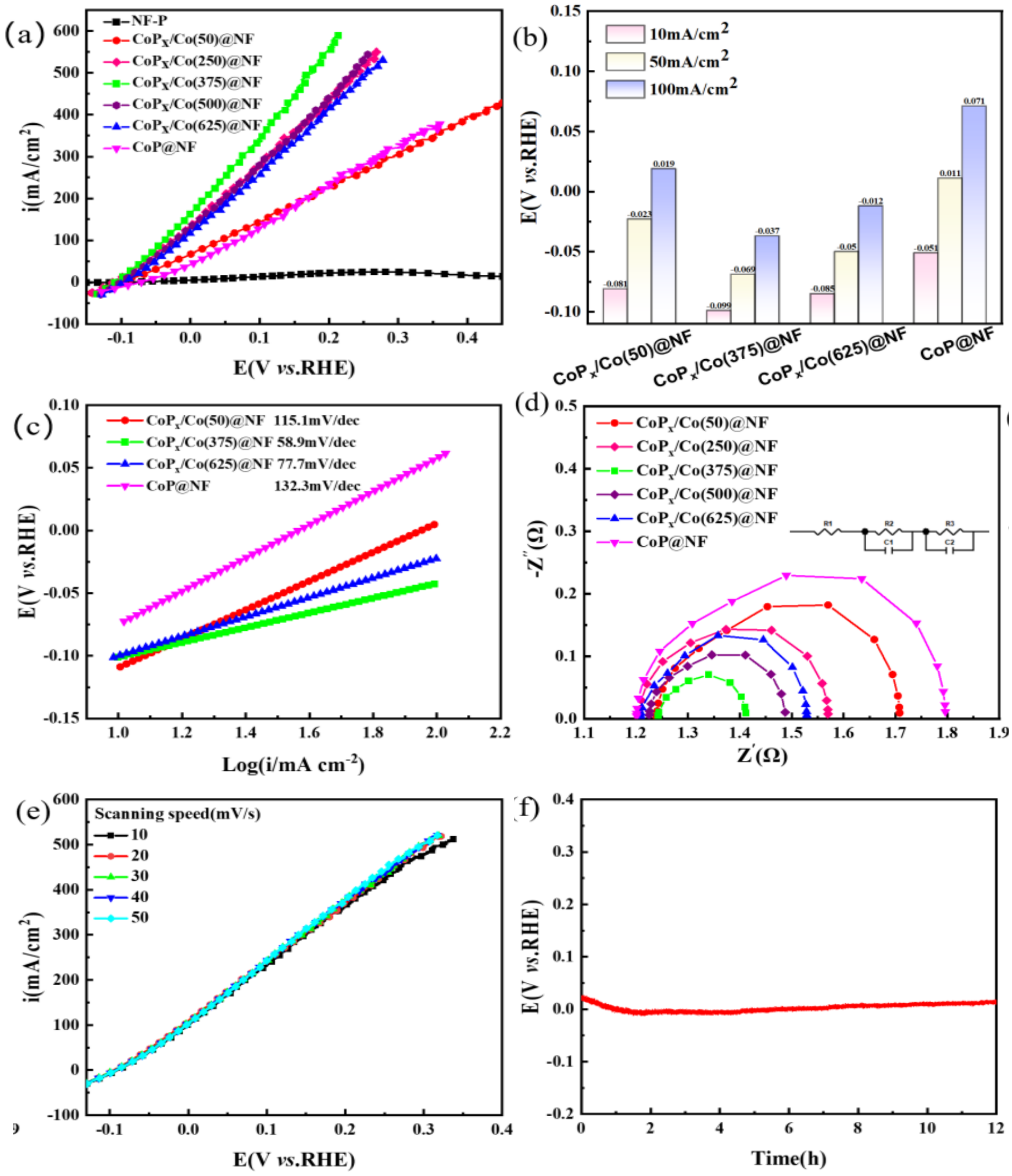

Figure 6. (a) LSV curves, (b) the potentials at the current density of 10, 50 and 100 $mA{\cdot}cm^{-2}$, (c) Tafel plots, and (d) EIS curves of the CoP@NF, $CoP_x/Co(x)$@NF and NF-P electrodes, (e) LSV curves of $CoP_x/Co(375)$@NF electrode at different scan rates in 0.2 M $N_2H_4{\cdot}H_2O$ + 1 M KOH solutio, (f) Catalytic stability of the $CoP_x/Co(375)$@NF electrode at 100 $mA{\cdot}cm^{-2}$ in 3 M $N_2H_4{\cdot}H_2O$ + 1 M KOH solution.

The comparison of the electrocatalytic activity toward HzOR of CoP_x/Co(375)@NF electrode with recently reported non-noble metal catalysts are listed in Table 2. With the recently reported catalysts compared, such as Ni_2P@NF (–25 mV@50 $mA\cdot cm^{-2}$) [38], Ni-NASA @NF (15 mV@50 $mA\cdot cm^{-2}$) [39], Ni-Co-P/NF(–24 mV@100 $mA\cdot cm^{-2}$) [32], FHNNP/NF (1 mV@100 $mA\cdot cm^{-2}$) [40] and PW-Co_3N/NF (–55 mV@10 $mA\cdot cm^{-2}$) [41], the optimized CoP_x/Co(375)@NF electrode exhibits obviously superior electrocatalytic activity toward HzOR.

Figure 6(d) shows the EIS curves of the electrodes in 0.2 M $N_2H_4\cdot H_2O$ + 1 M KOH solution. In the equivalent circuit model, R_1 represents the solution resistance, R_2 represents the instantaneous oxidation resistance of CoP_x and R_3 represents the charge transfer resistance associated with the hydrazine oxidation reaction (HzOR), C_1 and C_2 simulate the double-layer capacitance at the catalyst interface and the electrode/electrolyte interface, respectively [42,43]. The fitting equivalent circuit parameters of electrodes are presented in Table 3. It indicates that the R_2 and R_3 of the CoP_x/Co(x)@NF electrodes are all lower than those of the CoP@NF electrodes. This suggests that the CoP_x/Co heterostructure facilitates electron transfer, which reduces both the instantaneous oxidation resistance of CoP_x to $CoPO_x$ and the charge transfer resistance during the HzOR process. This significant reduction in transfer resistance greatly enhances the catalytic activity of the electrodes towards HzOR. Besides, as the influence of the cathodic current density concerned, the CoP_x/Co(375)@NF electrode also exhibits the lowest instantaneous oxidation resistance of CoP_x ($R_2 = 0.011\ \Omega$) and the lowest HzOR transfer resistance ($R_3 = 0.165\ \Omega$). However, as discussed before that CoP_x/Co heterojunction plays the key role for the catalytic activity, the oxidation of CoP_x to $CoPO_x$ exhibits no change in the catalytic activity toward the HzOR, which might be result from the strong reducibility of hydrazine hydrate, in situ electrochemically oxidized CoP_x/Co(x)@NF can be recovered back to active CoP_x species by $N_2H_4(CoPO_x) + N_2H_4 \rightarrow CoP_x + N_2 + H_2O$) [32].

Figure 6(e) shows the LSV curves of the CoP_x/Co(375)@NF sample in 0.2 M $N_2H_4\cdot H_2O$ + 1 M KOH solution at different scan rates and it can be seen the LSV curves does not undergo significant changes as the scan rate changes. This further indicates that the CoP_x/Co(375) @NF sample achieves effective charge and mass transfer at the solid-liquid-gas triphase interface between the electrode, electrolyte and reaction products N_2. This result is consistent with the EIS results and further validates that the nanoflower-like nanoarray structure facilitates rapid mass transfer.

Figure 6(f) presents the catalytic stability of the CoP_x/Co(375)@NF electrode at a current density of 100 $mA\cdot cm^{-2}$ in 3 M $N_2H_4\cdot H_2O$ + 1 M KOH solution. The chronoamperometry results show that the electrode potential remains stable over 12 h, with almost no obvious change in potential. This demonstrates the excellent catalytic stability toward HzOR of the CoP_x/Co(375)@NF electrode.

To further explore the catalytic mechanism of the CoP_x/Co structure for hydrazine oxidation, several electrochemical analyses were conducted. Figure 7(a) shows the LSV curves of the CoP_x/Co(375) @NF electrodes in 1 M KOH solution and in 0.2 M $N_2H_4\cdot H_2O$ + 1 M KOH solution. The difference between the LSV curves indicate that the current in 0.2 M $N_2H_4\cdot H_2O$ + 1 M KOH solutions originates from the oxidation of hydrazine.

The 1st and 200th cycles of the CV curves for the CoP_x/Co(375) @NF electrode in 1 M KOH solution are presented in Figure 7(b). The CV curves show an oxidation peak near 0.25 V in the first scan, which is associated with the oxidation of CoP_x to $CoPO_x$ [32]. As the number of CV scans increases, this oxidation peak gradually diminishes and completely disappears after 200 scans, indicating that the reaction is irreversible in KOH solution.

Table 2. Comparison of the electrocatalytic activity toward HzOR of CoPx/Co(375)@NF electrode with the recently reported catalysts.

Electrodes	**I [$mA\cdot cm^{-2}$]**	**E [mV]**	**Ref.**
CoP_x/Co(375)@NF	10	–99	This work
	50	–69	
	100	–37	
Ni_2P@NF	50	–25	38
Ni-NASA	50	15	39
Ni-Co-P/NF	10	–61	32
	100	–24	
FHNNP/NF	10	–44	40
	50	–12	
	100	1	
PW-Co_3N/NF	10	–55	41

Table 3. Equivalent circuit parameters of electrodes in 0.2 M $N_2H_4\cdot H_2O$ + 1 M KOH solution.

Electrodes	**R_1 [Ω]**	**R_2 [Ω]**	**R_3 [Ω]**	**C_1**	**n_1**	**C_2**	**n_2**
CoP_x/Co(50)@NF	1.230	0.047	0.440	0.337	0.644	0.078	0.852
CoP_x/Co(250)@NF	1.290	0.015	0.353	0.023	0.966	0.080	0.881
CoP_x/Co(375)@NF	1.240	0.011	0.165	0.049	1.090	0.139	0.883
CoP_x/Co(500)@NF	1.220	0.013	0.264	0.582	0.694	0.133	0.841
CoP_x/Co(625)@NF	1.285	0.015	0.316	0.0144	1.128	0.095	0.873
CoP@NF	1.210	0.075	0.588	0.784	0.784	0.080	0.803

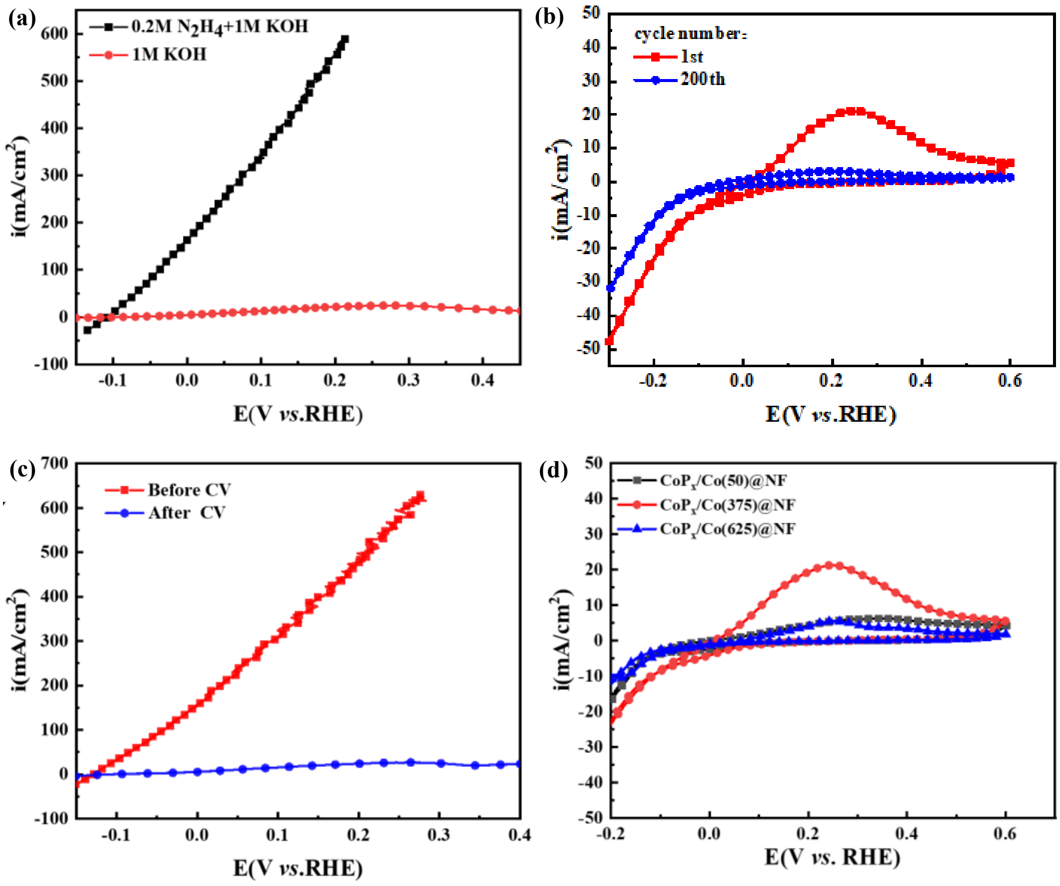

Figure 7. (a) LSV curves of the CoP_x/Co(375)@NF electrode in 1M KOH solution and in 0.2 M $N_2H_4 \cdot H_2O$ + 1 M KOH solution, (b) The 1st and 200th cycles of the CV curves for the CoP_x/Co(375) @NF electrode in 1 M KOH solution, (c) LSV curves of the CoP_x/Co(375)@NF electrode in 0.2 M $N_2H_4 \cdot H_2O$ + 1 M KOH solution before and after 200 cycles of CVs in 1 M KOH solution, (d) The 1st CV curves of CoP_x/Co(50)@NF, CoP_x/Co(375)@NF and CoP_x/Co(625)@NF electrodes in 1 M KOH solution.

LSV curves of the CoP_x/Co(375)@NF electrodes in 0.2 M $N_2H_4 \cdot H_2O$ + 1 M KOH solution before and after 200 cycles CVs in 1 M KOH solution are shown in Figure 7(c). The deactivation toward HzOR after 200 cycles CVs suggests that the catalytic activity toward HzOR of the CoP_x/Co(375)@NF is closely related to the instantaneous oxidation of CoP_x on the electrode surface. Excessive oxidation of CoP_x 1 M KOH solution results in the loss of the active sites. It may be concluded that the catalytic activity and stability toward HzOR might be relative with the area of the oxidation of CoP_x to $CoPO_x$ and the recoverability of $CoPO_x$ to CoP_x [32].

The electrochemical active surface area (EASA) reflects the intrinsic performance of the electrode, a larger EASA indicates more active sites available and better performance. In this system, the area of the oxidation of CoP_x to $CoPO_x$ can be used to characteristic the EASA. Figure 7(d) shows the first CV curves of CoP_x/Co(50)@NF, CoP_x/Co(375)@NF and CoP_x/Co(625)@NF electrodes in 1 M KOH solution. It shows that the CoP_x/Co(375)@NF electrode has the largest area for the oxidation of CoP_x to $CoPO_x$, indicating the highest EASA, which is consistent with its best catalytic activity toward HzOR. This might be attributed to two main factors. Firstly, the appropriate phosphidation degree of the CoP_x/Co(375)@NF electrode avoids insufficient phosphidation at low currents leads to less active sites and excessive phosphidation at high currents results in over-encapsulation of Co active sites by phosphates. Secondly, the porous nanoflower-like structure of the electrode facilitates the exposure of active sites.

4. Conclusion

In this study, a high-performance HzOR electrocatalyst was developed via a dual-component phosphidation strategy. By simply adjusting the cathodic current density, the composition and structure of the self-supported 3D nanoarray precursor Co/Co$(OH)_2$@NF were effectively regulated. Further leveraging the distinct phosphidation behaviors of metallic Co and $Co(OH)_2$, a tunable CoP_x/Co hetero-structure with controllable composition and structure was achieved. The optimal electrocatalytic performance was realized at a cathodic current density of 375 $mA \cdot cm^{-2}$. This can be attributed to several factors. Firstly, the CoP_x/Co(375)@NF electrode has an appropriate CoP_x/Co ratio, which prevents insufficient phosphidation at low currents (leading to a lack of active sites) and excessive phosphidation at high currents (resulting in over-encapsulation of Co active sites by CoP_x). Secondly, the porous nanoflower-like structure of the electrode facilitates the exposure of active sites, avoiding the aggregation and overlapping stacking of nanosheets that would otherwise reduce the utilization rate of active sites. This structure also promotes rapid mass transfer, significantly enhancing the electrode's performance at high current densities. Overall, this study provides a new strategy for further improving the catalytic performance toward HzOR.

References

[1] X. Zhao, Q. Feng, M. Liu, Y. Wang, W. Liu, D. Deng, J. Jiang, X. Zheng, L. Zhan, J. Wang, H. Zheng, Y. Bai, Y. Chen, X. Xiong, and Y. Lei, "Built-in electric field promotes interfacial adsorption and activation of CO_2 for C1 products over a wide potential window," *ACS Nano*, vol. 18, no. 13, pp. 9678-9687, 2024.

[2] X. Zhao, M. Liu, Y. Wang, Y. Xiong, P. Yang, J. Qin, X. Xiong, and Y. Lei, "Designing a built-in electric field for efficient energy electrocatalysis," *ACS Nano*, vol. 16, no. 12, pp. 19959-19979, 2022.

[3] D. Deng, J. Wu, Q. Feng, X. Zhao, M. Liu, Y. Bai, J. Wang, X. Zheng, J. Jiang, Z. Zhuang, X. Xiong, D. Wang, and Y. Lei, "Highly reversible zinc-air batteries at 40°C enabled by anion-mediated biomimetic fat," *Advanced Functional Materials*, vol. 34, no. 2, p. 2308762, 2024.

[4] M. A. Aminudin, S. K. Kamarudin, B. H. Lim, E. H. Majilan, M. S. Masdar, and N. Shaari, "An overview: Current progress on hydrogen fuel cell vehicles," *International Journal of Hydrogen Energy*, vol. 48, no. 11, pp. 4371-4388, 2023.

[5] A. Pramuanjaroenkij, and S. Kakac, "The fuel cell electric vehicles: The highlight review," *International Journal of Hydrogen Energy*, vol. 48, no. 25, pp. 9401-9425, 2023.

[6] N. Sazali, W. N. Wan Salleh, A. S. Jamaludin, and M. N. Mhd Razali, "New perspectives on fuel cell technology: A brief review," *Membranes*, vol. 10, no. 5, p. 99, 2020.

[7] P. Muthukumar, A. Kumar, M. Afzal, S. Bhogilla, P. Sharma, A. Parida, S. Jana, E. A. Kumar, R. K. Pai, and I. P. Jain, "Review on large-scale hydrogen storage systems for better sustainability," *International Journal of Hydrogen Energy*, vol. 48, no. 85, pp. 33223-33259, 2023.

[8] A. Raza, M. Arif, G. Glatz, M. Mahmoud, M. Al Kobaisi, S. Alafnan, and S. Iglauer, "A holistic overview of underground hydrogen storage: Influencing factors, current understanding, and outlook," *Fuel*, vol. 330, p. 125636, 2022.

[9] E. Rivard, M. Trudeau, and K. Zaghib, "Hydrogen storage for mobility: A review," *Materials*, vol. 12, no. 12, p. 1973, 2019.

[10] M. A. U. Din, M. Idrees, S. Jamil, S. Irfan, G. Nazir, M. A. Mudassir, M. S. Saleem, S. Batool, N. Cheng, and R. Saidur, "Advances and challenges of methanol-tolerant oxygen reduction reaction electrocatalysts for the direct methanol fuel cell," *Journal of Energy Chemistry*, vol. 77, pp. 499-513, 2023.

[11] J. Shi, Y. Zhu, Y. Feng, J. Yang, and C. Xia, "A prompt decarbonization pathway for shipping: Green hydrogen, ammonia, and methanol production and utilization in marine engines," *Atmosphere*, vol. 14, no. 3, p. 584, 2023.

[12] Z. Tian, Y. Wang, X. Zhen, and Z. Liu, "The effect of methanol production and application in internal combustion engines on emissions in the context of carbon neutrality: A review," *Fuel,* vol. 320, p. 123902, 2022.

[13] Y. Wang, Q. Cao, L. Liu, Y. Wu, H. Liu, Z. Gu, and C. Zhu, "A review of low and zero carbon fuel technologies: Achieving ship carbon reduction targets," *Sustainable Energy Technologies and Assessments*, vol. 54, p. 102762, 2022.

[14] W. Xu, Z. Lu, X. Sun, L. Jiang, and X. Duan, "Superwetting electrodes for gas-involving electrocatalysis," *Accounts of Chemical Research*, vol. 51, no. 7, pp. 1590-1598, 2018.

[15] K. Asazawa, K. Yamada, H. Tanaka, A. Oka, M. Taniguchi, and T. Kobayashi, "A platinum-free zero-carbon-emission easy fuelling direct hydrazine fuel cell for vehicles," *Angewandte Chemie-International Edition*, vol. 46, no. 42, pp. 8024-8027, 2007.

[16] N. Fujiwara, S.-i. Yamazaki, and K. Yasuda, "Research and development on direct polymer electrolyte fuel cells," *Journal of the Japan Petroleum Institute*, vol. 54, no. 4, pp. 237-247, 2011.

[17] E. Granot, B. Filanovsky, I. Presman, I. Kuras, and F. Patolsky, "Hydrazine/air direct-liquid fuel cell based on nanostructured copper anodes," *Journal of Power Sources*, vol. 204, pp. 116-121, 2012.

[18] K. Yamada, K. Yasuda, N. Fujiwara, Z. Siroma, H. Tanaka, Y. Miyazaki, and T. Kobayashi, "Potential application of anion-exchange membrane for hydrazine fuel cell electrolyte," *Electrochemistry Communications*, vol. 5, no. 10, pp. 892-896, 2003.

[19] K. Pang, Y. Tang, C. Qiu, M. Zhang, A. Tayal, S. Feng, C. Long, Y. Wang, J. Chang, B. Pang, A. Sikdar, S. S. Garakani, Y. Zhang, H. Wang, W. Zhang, G. Luo, Y. Wang, and J. Yuan, "Redirecting configuration of atomically dispersed selenium catalytic sites for efficient hydrazine oxidation," *Matter*, vol. 7, no. 2, pp. 655-667, 2024.

[20] J. Zhou, X. Meng, R. Zhang, H. Liu, and Z. Liu, "Progress on electrodeposition of rare earth metals and their alloys," *Electrocatalysis*, vol. 12, no. 6, pp. 628-640, 2021.

[21] K. Yamada, K. Asazawa, K. Yasuda, T. Ioroi, H. Tanaka, Y. Miyazaki, and T. Kobayashi, "Investigation of PEM type direct hydrazine fuel cell," *Journal of Power Sources*, vol. 115, no. 2, pp. 236-242, 2003.

[22] X. Gao, K. Lu, J. Chen, J. Min, D. Zhu, and M. Tan, "NiCoP-CoP heterostructural nanowires grown on hierarchical Ni foam as a novel electrocatalyst for efficient hydrogen evolution reaction," *International Journal of Hydrogen Energy*, vol. 46, no. 45, pp. 23205-23213, 2021.

[23] S. Chen, C. Wang, S. Liu, M. Huang, J. Lu, P. Xu, H. Tong, L. Hu, and Q. Chen, "Boosting hydrazine oxidation reaction on CoP/Co mott-schottky electrocatalyst through engineering active sites," *Journal of Physical Chemistry Letters*, vol. 12, no. 20, pp. 4849-4856, 2021.

[24] Y. Zhang, Y. Qiu, Z. Ma, Y. Wang, Y. Zhang, Y. Ying, Y. Jiang, Y. Zhu, and S. Liu, "Core-corona Co/CoP clusters strung on carbon nanotubes as a Schottky catalyst for glucose oxidation assisted H2 production," *Journal of Materials Chemistry A*, vol. 9, no. 17, pp. 10893-10908, 2021.

[25] T. Liu, P. Li, N. Yao, G. Cheng, S. Chen, W. Luo, and Y. Yin, "CoP-Doped MOF-based electrocatalyst for pH-universal hydrogen evolution reaction," *Angewandte Chemie International Edition*, vol. 58, no. 14, pp. 4679-4684, 2019.

[26] H. H. Zhang, G. S. Han, Y. Y. Liu, L. L. Zhao, W. B. Zhang, M. T. Khalil, H. J. Wei, C. M. Wang, T. Liu, X. J. Guo, X. L.

Wu, J. C. Jiang, and B. J. Li, "CoP/Co heterojunction on porous g-C_3N_4 nanosheets as a highly efficient catalyst for hydrogen generation," *Journal of Colloid and Interface Science*, vol. 658, pp. 22-31, 2024.

[27] Z. Lu, Y. Cao, J. Xie, J. Hu, K. Wang, and D. Jia, "Construction of Co_2P/CoP@Co@NCNT rich-interface to synergistically promote overall water splitting," *Chemical Engineering Journal,* vol. 430, p. 132877, 2022.

[28] J. S. Santos, F. Trivinho-Strixino, and E. C. Pereira, "Investigation of $Co(OH)_2$ formation during cobalt electrodeposition using a chemometric procedure," *Surface and Coatings Technology*, vol. 205, no. 7, pp. 2585-2589, 2010.

[29] Z. Yu, Z. Cheng, S. R. Majid, Z. Tai, X. Wang, and S. Dou, "Smart design of free-standing ultrathin Co–$Co(OH)_2$ composite nanoflakes on 3D nickel foam for high-performance electrochemical capacitors," *Chemical Communications*, vol. 51, no. 9, pp. 1689-1692, 2015.

[30] F. Su, C. Liu, J. Guo, and P. Huang, "Characterizations of nanocrystalline Co and Co/MWCNT coatings produced by different electrodeposition techniques," *Surface and Coatings Technology*, vol. 217, pp. 94-104, 2013.

[31] X. Wu, M. Liu, Z. Jiang, J. Li, K. Song, A. Wei, D. Meng, T. Dong, Z. Gao, W. Zhang, and W. Zheng, "Electrodeposition-potential tuning rejuvenates the concurrent preparation from α-$Co(OH)_2$ with larger interlayer‐spacings to β-$Co(OH)_2$," *Batteries & Supercaps,* p. e202400699, 2025.

[32] L. Zhu, J. Huang, G. Meng, T. Wu, C. Chen, H. Tian, Y. Chen, F. Kong, Z. Chang, X. Cui, and J. Shi, "Active site recovery and N-N bond breakage during hydrazine oxidation boosting the electrochemical hydrogen production," *Nature Communications*, vol. 14, no. 1, p. 1997, 2023.

[33] J. Zhou, S.-f. Wang, and X.-s. Song, "Electrodeposition of cobalt in double-membrane three-compartment electrolytic reactor," *Transactions of Nonferrous Metals Society of China*, vol. 26, no. 6, pp. 1706-1713, 2016.

[34] C. Yue, N. Zhang, Z. Zhu, P. Chen, F. Meng, X. Liu, X. Wei, and J. Liu, "Multi-strategy architecture of high‐efficiency electrocatalysts for underwater Zn–H_2O_2 batteries with superior power density of 442 $mW\cdot cm^{-2}$," *Small*, vol. 18, no. 12, p. 2106532, 2022.

[35] L.-M. Cao, Y.-W. Hu, S.-F. Tang, A. Iljin, J.-W. Wang, Z.-M. Zhang, and T.-B. Lu, "Fe-CoP electrocatalyst derived from a bimetallic prussian blue analogue for large-current-density oxygen evolution and overall water splitting," *Advanced Science*, vol. 5, no. 10, p. 1800949, 2018.

[36] N. Bai, Q. Li, D. Mao, D. Li, and H. Dong, "One-Step electrodeposition of Co/CoP film on Ni foam for efficient hydrogen evolution in alkaline solution," *ACS Applied Materials & Interfaces*, vol. 8, no. 43, pp. 29400-29407, 2016.

[37] M. Deng, H. Yang, L. Peng, L. Zhang, L. Tan, G. He, M. Shao, L. Li, and Z. Wei, "Insight into the boosted activity of TiO_2-CoP composites for hydrogen evolution reaction: Accelerated mass transfer, optimized interfacial water, and promoted intrinsic activity," *Journal of Energy Chemistry*, vol. 74, pp. 111-120, 2022.

[38] C. Tang, R. Zhang, W. Lu, Z. Wang, D. Liu, S. Hao, G. Du, A. M. Asiri, and X. Sun, "Energy-saving electrolytic hydrogen generation: Ni_2P nanoarray as a high-performance non-noble-metal electrocatalyst," *Angewandte Chemie International Edition*, vol. 56, no. 3, pp. 842-846, 2016.

[39] Y. Kuang, G. Feng, P. Li, Y. Bi, Y. Li, and X. Sun, "Single-crystalline ultrathin nickel nanosheets array from in situ topotactic reduction for active and stable electrocatalysis," *Angewandte Chemie International Edition*, vol. 55, no. 2, pp. 693-697, 2015.

[40] S. Zhang, X. Wei, S. Dai, H. Wang, and M. Huang, "Efficient hydrazine electro‐oxidation achieved by tailored electron injection into Fe(III) sites activating dehydrogenation," *Advanced Functional Materials*, vol. 34, no. 10, p. 2311370, 2023.

[41] Y. Liu, J. Zhang, Y. Li, Q. Qian, Z. Li, Y. Zhu, and G. Zhang, "Manipulating dehydrogenation kinetics through dual-doping Co_3N electrode enables highly efficient hydrazine oxidation assisting self-powered H_2 production," *Nature Communications*, vol. 11, no. 1, p. 1853, 2020.

[42] Y. Bai, D. Deng, J. Wang, Y. Wang, Y. Chen, H. Zheng, M. Liu, X. Zheng, J. Jiang, H. Zheng, M. Yi, W. Li, G. Fang, D. Wang, and Y. Lei, "Inhibited passivation by bioinspired cell membrane Zn interface for Zn-Air batteries with extended temperature adaptability," *Advanced Materials*, vol. 36, no. 40, p. 2411404, 2024.

[43] Y. Chen, H. Yao, F. Kong, H. Tian, G. Meng, S. Wang, X. Mao, X. Cui, X. Hou, and J. Shi, "V_2C MXene synergistically coupling FeNi LDH nanosheets for boosting oxygen evolution reaction," *Applied Catalysis B: Environmental*, vol. 297, p. 120474, 2021.